# A Multiwavelet Treatment of the Quantum Subsystem in Quantum Wavepacket *Ab Initio* Molecular Dynamics through an Hierarchical Partitioning of Momentum Space

Alexander H. Prociuk and Srinivasan S. Iyengar*

Department of Chemistry and Department of Physics, Indiana University, Bloomington, Indiana 47405, United States

S *Supporting Information*

ABSTRACT: We present an hierarchical scheme where the propagator in quantum dynamics is represented using a multiwavelet basis. The approach allows for a recursive refinement methodology, where the representation in momentum space can be adaptively improved through additional, decoupled layers of basis functions. The method is developed within the constructs of quantum-wavepacket ab initio molecular dynamics (QWAIMD), which is a quantum-classical method and involves the synergy between a time-dependent quantum wavepacket description and ab initio molecular dynamics. Specifically, the

current development is embedded within an "on-the-fly" multireference electronic structural generalization of QWAIMD. The multiwavelet treatment is used to study the dynamics and spectroscopy in a small hydrogen bonded cluster. The results are in agreement with previous calculations and with experiment. The studies also allow an interpretation of the shared proton dynamics as one that can be modeled through the dynamics of dressed states.
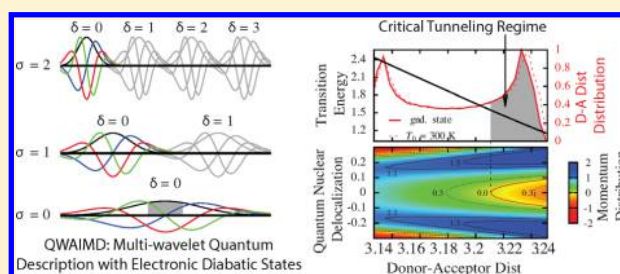
I. INTRODUCTION

Recently,[1−13] we introduced a methodology that accurately computes quantum dynamical effects in a subsystem while simultaneously treating the motion of the surrounding atoms and coupled changes in electronic structure. The approach is quantum-classical[14−25] and involves the synergy between a time-dependent quantum wavepacket description and *ab initio* molecular dynamics. As a result, the approach is called quantum-wavepacket *ab initio* molecular dynamics (QWAIMD). Since the quantum dynamics was performed on a grid, the predominant bottleneck was the computation of the grid-based, time-dependent electronic structure potential and gradients generated by the motion of the classical nuclei.[1−4,6,7,9] This limitation was partially surmounted through the following methodological improvements:

(a) A time-dependent deterministic sampling (TDDS) technique was introduced in refs 3, 4, and 9, which, when combined with numerical methods such as an efficient wavelet compression scheme and low-pass filtered Lagrange interpolation,[4] provides computational gains of many orders of magnitude. In the language of finite-element-methods used in computational mechanics, it may be noted that the TDDS method is an adaptive (*space- and time-dependent*) *h*-type mesh refining technique.[26] In TDDS, the mesh refinement is performed through a sampling function constructed using quantum dynamics data such as wavepacket density, potential, potential gradient and the Shannon entropy associated with the wavepacket density.[4,9]

(b) Multiple diabatic reduced single particle electronic density matrices were propagated simultaneously with the

quantum wavepacket in refs 6 and 7, and the associated diabatic states were used to construct an adiabatic surface at every instant in time using a nonorthogonal CI formalism. Each diabatic state is strongly correlated with a given region within the quantum vibrational configuration space. This allows for these states to be selected based on the level of influence that their electronic correlations contribute to the electronic-vibrational coupling within the quantum wavepacket. Furthermore, the diabatic approximation allowed reuse of the two-electron integrals during the on-the-fly potential energy surface computation stage on account of the limited dependence of the diabatic electronic state functions on the quantum nuclear coordinate. This leads to substantial reductions in computational time. QM/MM and QM/QM generalizations[5] and extensions to periodic condensed phase systems[8] have also been explored. We have utilized QWAIMD to compute vibrational properties of hydrogen-bonded clusters inclusive of quantum nuclear effects[4,6,7] and have also adopted the method to study hydrogen tunneling in enzyme active sites.[10,27,28] The quantum dynamics scheme in QWAIMD has also been used to develop a technique known as multistage *ab initio* wavepacket dynamics (MSAIWD) to treat open, nonequilibrium electronic systems.[12,13]

However, several challenges remain:

(i) Because of the expense involved in on-the-fly dynamics, currently, it is only possible to treat a few (three or less)

quantum nuclear degrees that are coupled to a set of classical particles.

(ii) Dynamics of the order of several picoseconds is possible, but longer time-scale dynamics is expensive. In this regard, initial developments toward a rare-events sampling scheme have been completed.[28]

(iii) Currently, it is only possible to study QWAIMD using moderately accurate electronic structure methods, such as hybrid density functional theory. Again, in this regard, initial developments that include the effect of multiple electronic state functions have been considered in refs 6 and 7.

Of the challenges listed above, the current publication will focus on improvements to the quantum dynamics scheme used in QWAIMD. That is, the possibility of compressing the information content of the vibrational wave packet during its propagation is explored independent of how the underlying electronic structure is computed. To this end, a multiwavelet-based representation of the quantum nuclear wavepacket is considered as a replacement for the grid basis used in QWAIMD.[29−37] The multiwavelet structure allows for a layered partitioning (or filtering) of the Fourier space representation of the time-dependent quantum nuclear wavepacket. By adaptively considering layers that appear significant in the Fourier representation, we tailor the dynamics to be stable and efficient. The multiwavelet primitives are chosen to have analytically known free-propagated forms as well as derivatives, as is already the case with "distributed approximating functionals".[38,39] This reduces the overhead in computing matrix elements for the Hamiltonian and propagator. Furthermore, the method is fully integrated with our recently developed MC-QWAIMD to provide the time-dependent potential surface for quantum nuclear treatment.

The paper is organized as follows. A brief review of grid based quantum wavepacket propagation implemented within the QWAIMD methodology is provided in section II. Sections III and IV, together, introduce the multiwavelet-based representation of the quantum nuclear wavepacket. Numerical benchmarks are provided in sections V and VI. Specifically, section V involves an exhaustive search of the parameter space within the multiwavelet protocol, which allows us to examine and develop the multiwavelet basis toward tailored accuracy and efficiency. In section VI, an approach is used to study the dynamics in a hydrogen-bonded bihalide system. It is found that the results agree well with previous studies. Conclusions are given in section VII.

II. A BRIEF OVERVIEW OF GRID-BASED QUANTUM WAVEPACKET PROPAGATION IN QUANTUM WAVEPACKET *AB INITIO* MOLECULAR DYNAMICS (QWAIMD)

We provide a brief review of the grid-based quantum dynamics methods currently implemented for wavepacket propagation within QWAIMD before we engage in further discussion. More details can be seen in refs 1−4, 6, and 8. The main features are as follows: The quantum dynamical evolution is described through a third-order Trotter factorization of the quantum propagator,[1,40−42] where the free-propagator is approximated in the coordinate representation using a formally exact expression known as the "distributed approximation functional" (DAF):[1,2,38,39,43,44]

$$\left\langle R_{QM} \left| \exp\left\{ -\frac{\iota K \Delta t}{\hbar} \right\} \right| R'_{QM} \right\rangle_{DAF} \equiv \tilde{K}(R_{QM} - R'_{QM}, M_{DAF}, \sigma', \Delta t)$$

$$= \frac{1}{\sigma'(0)} \sum_{n=0}^{M_{DAF}/2} \left(\frac{\sigma'(0)}{\sigma'(\Delta t)} \right)^{2n+1} \left(\frac{-1}{4} \right)^n \times \frac{1}{n!} (2\pi)^{-1/2}$$

$$\exp\left\{ -\frac{(R_{QM} - R'_{QM})^2}{2\sigma'(\Delta t)^2} \right\} \times H_{2n}\left(\frac{R_{QM} - R'_{QM}}{\sqrt{2}\,\sigma'(\Delta t)} \right) \quad (1)$$

Here, $\{\sigma'(\Delta t)\}^2 = \sigma'(0)^2 + i\Delta t\hbar/M_{QM}$, $\{H_{2n}(x)\}$ are even-ordered Hermite polynomials (note that the arguments for the Hermite polynomials and the Gaussian function, $[(R_{QM} - R'_{QM})/(\sqrt{2}\sigma'(\Delta t))]$, are generally complex) and R_{QM} represents the quantum mechanical degrees of freedom. The right side of eq 1 is related to the multiwavelet, frame description of nuclear wave functions that is used in the current publication. The free-propagation of a wavepacket is then given in the discrete coordinate representation as

$$\chi(R_{QM}^i, \Delta t) = \Delta x \sum_j \langle R_{QM}^i| \exp\{-\iota K\Delta t/\hbar\}|R_{QM}^j\rangle \chi(x_j, 0)$$

$$= \Delta x \sum_j \tilde{K}(R_{QM}^i - R_{QM}^j, M_{DAF}, \sigma', \Delta t)\chi(R_{QM}^j, 0)$$

$$(2)$$

The parameters M_{DAF} and σ' above, together[1,39] determine the accuracy and efficiency of the DAF-propagator. As M_{DAF} increases, the accuracy as well as the computational expense increase.

It is worth noting a few characteristics of eq 1. For any fixed level of approximation, determined by the choice of parameters M_{DAF} and $\sigma'(0)$, the kernel in eq 1 only depends on the quantity $(R_{QM}^i - R_{QM}^j)$ that is the distance between points in the coordinate representation and goes to zero as this quantity becomes numerically large on account of the Gaussian dependence. This yields a banded, Toeplitz matrix approximation to eq 1, for any finite M_{DAF} and $\sigma'(0)$. [The (i, j)-th element of a Toeplitz matrix depends only on $|i − j|$.] Because of these properties, eq 1 provides great simplicity in computation of the quantum propagation. One may contrast this idea with propagators found in standard real-time Feynman path integration, where the highly oscillatory nature of the integrand leads to a difficult numerical problem.[45] In fact, as shown in ref 13, it is possible to computationally implement the DAF propagation scheme in a form that includes a series of scalar-vector operations with the total number of operations given by

$$N + \sum_{i=1}^{W-1} 2(N - i) = N(2W - 1) - W(W - 1) \approx O(N)$$

$$(3)$$

where W is the width of the propagator in the coordinate representation, i.e., the maximum value of $(R_{QM}^i - R_{QM}^j)/\Delta x$ in eq 2 such that all values of the free propagator are less than a numerical threshold for $(R_{QM}^i - R_{QM}^j)/\Delta x > W$. Since W is not dependent on N [W, in fact, depends on M_{DAF} and $\sigma'(0)$, which is the required accuracy of propagation], this scaling goes as $O(N)$ for large grids. In this publication, we analyze whether such a scaling can be reduced further without sacrificing too much accuracy.

III. A GENERAL VIBRATIONAL WAVEPACKET ANSATZ

We begin by expressing the vibrational wavepacket, $\Psi^{(QM)}(\mathbf{R}_{QM}; t)$ as a fully correlated multiconfigurational expansion of one-dimensional functions, $\phi_{l,k_l}(R_{QM,l} - R^0_{QM,l})$:

$$\Psi^{(QM)}_j(\mathbf{R}_{QM}; t) = \sum_k d^{[j]}_k(t)\left[\prod^d_{l=1}\phi_{l,k_l}(R_{QM,l} - R^0_{QM,l})\right]$$

$$= \sum_k d^{[j]}_k(t)\Upsilon_k(\mathbf{R}_{QM}) \tag{4}$$

where the relevant degrees of freedom for all quantum nuclei are given by the d-dimensional vector $\mathbf{R}_{QM} = (R_{QM,1}, ..., R_{QM,d})$. For example, $\{R_{QM,l}: l = 1, ..., d\}$ can contain all spatial dimensions for every quantum nucleus, or a transformation of some subset therein. Thus, d defines the full dimensionality of the quantum nuclear problem being considered. The vector index, $\mathbf{k} = (k_1, ..., k_d)$ with k_l denoting indices on the one-dimensional basis functions $\phi_{l,k_l}(R_{QM,l} - R^0_{QM,l})$. The index $[j]$ represents the electronic state (adiabatic or diabatic); however, in this publication, we consider only adiabatic effects (that is, $j = 0$). Vibronic treatment is deferred to a future publication, since it involves developmental interplay between the electronic and vibrational motions. To simplify the notation, we have also introduced the Hartree product of one-dimensional functions:

$$\Upsilon_k(\mathbf{R}_{QM}) \equiv \prod^d_{l=1}\phi_{l,k_l}(R_{QM,l} - R^0_{QM,l}) \tag{5}$$

To effect a Fourier-space filtered multiresolution of $\Psi^{(QM)}_i$ that allows the function to maintain spatial and temporal amorphous features, the one-dimensional functions, $\phi_{l,k_l}(R_{QM,l} - R^0_{QM,l})$, are chosen as a linear combination of multi-wavelets,[29−37,46,47] as described in the next section. Matrix elements of the Hamiltonian and the propagator are considered in sections IV(C1), IV(C2), and IV(D).

IV. INTRODUCTION OF A PRIMITIVE BASIS CONSTRUCTED FROM MULTIWAVELETS TO REPRESENT $\phi_{l,k_l}(R_{QM,l} - R^0_{QM,l})$

As outlined in Section II, in the previous QWAIMD publications,[1−13] the quantum dynamics was performed on a grid representation. The potential surface was obtained on a compressed subset of grid points adaptively determined using a time-dependent sampling scheme.[3,4,9] In this publication, we represent the spatially amorphous behavior of the quantum wavepacket, $\Psi^{(QM)}_j$, by reducing errors associated with high levels of spatial localization. Discrete, localized basis set structures that satisfy this criterion include the wavelets,[29−31,46,47] Weyl-Heisenberg, or Gabor[30,31,47−54] (e.g., windowed Fourier functions), and multiwavelet[30,32−37] frames[29−31,46−58] with their structural properties having been studied extensively (see, for example, refs 59−61). Of these, we investigate the suitability of the multiwavelet frame, as it incorporates useful properties of both wavelet and Weyl-Heisenberg frames. Furthermore, the basis functions are chosen to be continuous with analytically known derivatives and free-propagated forms, as noted earlier. This simplifies propagation and computation of matrix elements (see section IV(A)).

We first introduce a one-dimensional set of multiwavelet functions, $\{\phi_{\mu,\sigma,\delta}\}$, the elements of which are used to construct
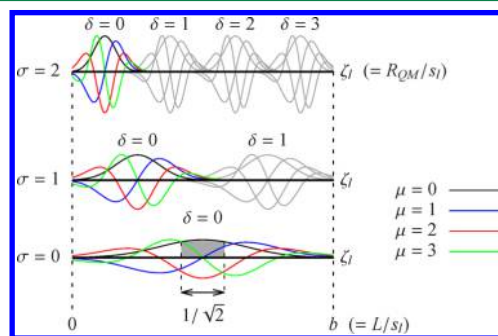

Figure 1. Multiwavelet primitives versus dimensionless position, ζ_l for the case where $a = 2$ and $b = 6/\sqrt{2}$, with highest generation, $\sigma_{max} = 2$, and number of basis functions per generation and translate, $\mu_{max} = 4$. The multiwavelet functions of differing order (modulation), μ, for the leftmost translate in each generation are distinguished by color. The functions ϕ_μ, from which the wavelet structure is generated via translation and dilation, correspond to the multiwavelets at $\sigma = 0$. The quantum nuclear position, R_{QM}, is scaled to ζ_l by the parameter s_l. The standard width of ϕ_0 is $1/\sqrt{2}$ in the ζ_l representation ($s_l/\sqrt{2}$ in the R_{QM} representation). The domain interval length is b in the ζ_l representation (L in the R_{QM} representation). The area under ϕ_0, corresponding to its standard width, is highlighted in gray.

the basis $\{\phi_{l,k_l}\}$ in eqs 4 and 5. As illustrated in Figure 1, a multiwavelet frame basis set is generated by sequentially applying translations and dilations to a set of windowed modulated basis functions ϕ_μ:

$$\phi_{\mu,\sigma,\delta}(\zeta_l) \equiv \phi_\mu\left(a^\sigma\zeta_l + b\left(\delta + \frac{1}{2}\right)\right)$$

$$= \phi_\mu\left(a^\sigma\left[\zeta_l + \frac{b}{a^\sigma}\left(\delta + \frac{1}{2}\right)\right]\right) \tag{6}$$

where ζ_l is a unitless position variable and b is the unitless interval of compact support. The non-negative integers δ, σ, and μ characterize the translate, scale, and modulation, respectively, of the given multiwavelet function. The dimensionless distance between two adjacent translates in generation σ is b/a^σ. The predetermined *wavelet* structural parameter, a, defines the scale or "dilation" factor. In addition, the ratio between the number of wavelet primitives in generation $\sigma + 1$ and the number of wavelet primitives in generation σ, is also a, as readily seen from the second equality in eq 6. Thus, the number of translates, δ_{max}, allowed within a spatial domain b for generation σ is the floor of a^σ, i.e. $\lfloor a^\sigma \rfloor$, which, for cases where a is an integer, reduces to a^σ. It is sometimes useful to introduce a fourth integer Λ to distinguish functions of even ($\Lambda = 1$) and odd ($\Lambda = -1$) reflection symmetry. The even functions are often referenced as *scales* while the odd functions are referenced as *wavelets*. However, this distinction is irrelevant to the current work and, hence, the Λ index is omitted from eq 6. In its place, we have the more exhaustive modulation index (μ). Generally the odd values of μ correspond to $\Lambda = -1$ and 1 otherwise. [The modulation parameter, μ, is discussed further below.] Finally, although the number of wavelet primitives (eq 6) may be extended arbitrarily in theory, the basis set is, in practice, truncated to a finite number of elements. Since the number of translates

Table 1. Comparisons of Total Energies, Flux and Donor−Acceptor Distance (for a Given Measurable Quantity, $O(t)$ (i.e., Total Energy, $O(t) = E(t)$; Shared Proton Flux, $O(t) = J(t)$; Cl−Cl Stretch, $O(t) = R_{Cl-Cl}(t)$), $\sigma[O]$ is the Standard Deviation of $O(t)$ over the Simulation Duration and $\Delta[O]$ is the 2-norm of the Difference between the Wavelet and Grid Propagated Measurable Quantities (O_{wav} and O_{DAF} Respectively), as Defined by eq 33[a]

	N_{DM}[b]	$\Delta[E]$	$\sigma[E_{wav}]$	$\sigma[E_{DAF}]$	$\sigma[J]_{wav}$	$(\Delta[J]/\sigma[J]_{wav})$	$\sigma[R_{Cl-Cl}]_{wav}$	$\Delta[R_{Cl-Cl}]/[R_{Cl-Cl}]_{wav}$
1D	5[c]	4.28×10^{-5}	0.0556	0.0572	2.04×10^{-9}	0.127	0.03	0.0198
	5[d]	4.34×10^{-5}	0.0563	0.0578	1.48×10^{-4}	0.011	0.03	0.0198
	9[c]	2.13×10^{-5}	0.0568	0.0605	1.88×10^{-9}	0.252	0.04	0.0647
	9[d]	2.05×10^{-5}	0.0578	0.0615	1.62×10^{-4}	0.182	0.04	0.0661
3D	9[c]	3.62×10^{-5}	0.0811	0.0836	1.18×10^{-8}	1.092	0.04	0.0226

[a]Energies are given in kcal/mol; flux in atomic units; distances in Angstroms. [b]Defined in eq 21. [c]Ground-state initial wave function (see eqs 28 and 29). [d]Thermal initial wave function (see eqs 28 and 30 with $T_0 = 300$ K).

varies with generation (Figure 1), we need only limit the highest generation to σ_{max} and the number of basis functions per generation and translate to μ_{max}. Figure 1 illustrates a truncated basis set corresponding to $\sigma_{max} = 2$ and $\mu_{max} = 4$. We will often refer to a given truncated basis set, using the ordered pair notation, $(\sigma_{max}, \mu_{max})$.

As with wavelets, the spatial domains of $\phi_{\mu,\sigma,\delta}$ scale with their wavelengths, which decrease by factors of a^σ with scale σ. Hence, the multiwavelet set can be used in constructing a multiresolution analysis of the function space and may reduce the spectral delocalization error commonly associated with delocalized modulated basis sets such as Fourier transforms. See, for example, refs 57, 62−67, where wavelet-type basis functions (such as those used here) have been benchmarked[62,63] and found to compare favorably with other propagation methods (see Table 1 in refs 62 and 63 for benchmarks and the appendix in ref 13 for computational scaling). Also see ref 68 for a discussion on the correspondence between the Gaussian basis functions used in electronic structure theory[69] and noninteger scale multiwavelets. Furthermore, multidimensional basis functions, which are constructed from single dimensional (multi)wavelets, are well-suited for treating spatially anisotropic wavepackets due to the flexibility introduced by both local scaling and translation. However, scaling and translation alone do not guarantee that the basis set will adequately span the momentum space of the wave packet, given the exponential dependence of the wavelength on the scaling parameter σ. Hence, in contrast to wavelets where the modulation parameter $\mu \leq 2$, the underlying Weyl-Heisenberg frame can contain as many functions ϕ_μ as is necessary to properly span the momentum space of the wave packet.

To shed light on the complementarity between scaling and modulation, it is useful to explore the properties of the multiwavelet functions in the Fourier domain. Figure 2 provides the squared absolute value of the k-space representation of a selection of multiwavelet functions (i.e., $|\mathcal{F}[\phi_{\mu,\sigma,\delta}](k)|^2$), where

$$\mathcal{F}[\phi_{\mu,\sigma,\delta}](k) \equiv \int d\zeta \, e^{-ik\zeta} \phi_{\mu,\sigma,\delta}(\zeta)$$

$$= \frac{A_\mu \sqrt{\pi}}{a^\sigma} \left(\frac{ik}{a^\sigma}\right)^\mu e^{ikb[\delta+(1/2)]/a^\sigma} \exp\left[-\frac{1}{4}\left(\frac{k}{a^\sigma}\right)^2\right] \tag{7}$$

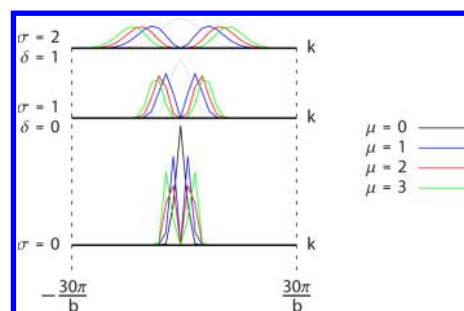As can be seen here, the multiwavelets act as band-pass filters with bandwidth, scaling as

Figure 2. Squared absolute value of selected multiwavelets represented in k-space (i.e., $|\mathcal{F}[\phi_{\mu,\sigma,\delta}](k)|^2$ where $\mathcal{F}[\phi_{\mu,\sigma,\delta}](k)$ is given by eq 7). Dashed curve in a given generation σ corresponds to a wavelet with a band-pass window that can be refined by substituting the wavelets from lower generations in its place.

$$\Delta k \approx a^\sigma \sqrt{\mu + \frac{1}{2}} \tag{8}$$

and band peaks given by

$$k^{(0)}_{\mu,\sigma} = \frac{\sqrt{2\mu} \, a^\sigma}{s_l} \tag{9}$$

for multiwavelet $\phi_{\mu,\sigma,\delta}$. Loosely, the modulation index μ governs band filter position while σ governs bandwidth. Moreover, in a given generation, σ, the lowest order wavelet, corresponding to $\mu = 0$, centered around $k = 0$ (and represented by a dotted curve in Figure 2), may be replaced by the wavelets of generation $\sigma - 1$, producing a band-pass refinement at lower k values in both band peak position and bandwidth. This refinement may be repeated iteratively at every generation $\sigma' < \sigma$, as needed, for finer momentum band filtering as $k \to 0$. This refinement is lost for intervals of high wavenumber, k, as the bandwidth scales like the band peak positions (see eqs 8 and 9). We note that the subset of multiwavelets presented in Figure 2 is representative of k-space population distributions for all free propagated and unpropagated basis functions within the set $(\sigma_{max}, \mu_{max}) = (2,4)$. This consequence arises from the fact that translation and free propagation only introduce linear and quadratic phase shifts, respectively, in this representation.

A. Propagated Forms of $\{\phi_{\mu,\sigma,\delta}\}$ That Are Used To Construct Matrix Elements. In addition to spatial localization, we require the functions $\phi_{\mu,\sigma,\delta}$ to be continuous with analytically known derivatives and free propagated forms. These requirements are satisfied by choosing Hermite functions,
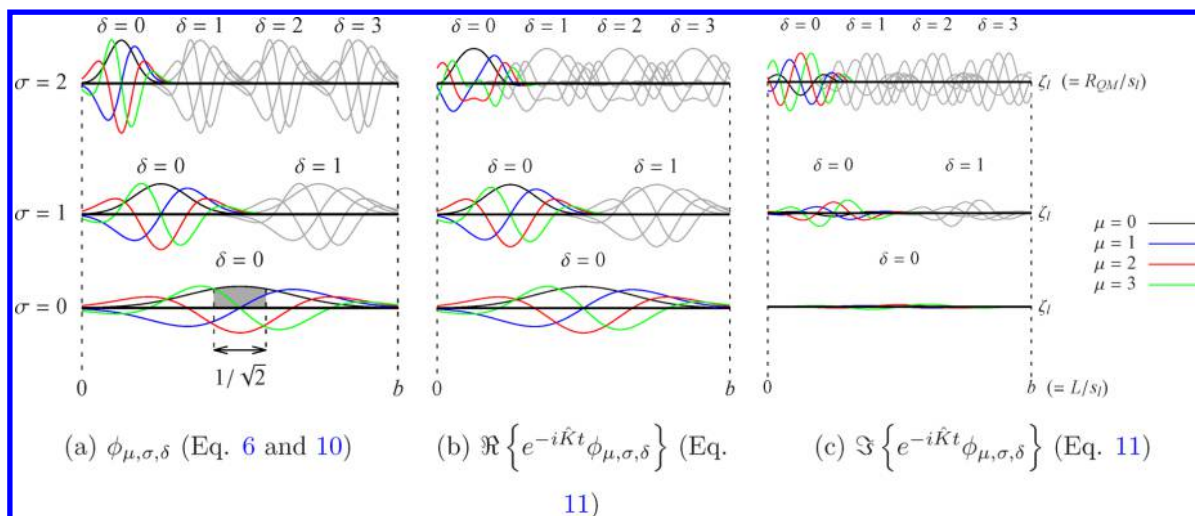
Figure 3. (a) Unpropagated multiwavelet basis (as in Figure 1) (b) Real and (c) imaginary components of free propagated multiwavelets for $t = 0.1$ fs.

$$\phi_\mu(\zeta_l) = (-1)^\mu A_\mu \frac{d^\mu}{d\zeta_l^\mu} e^{-\zeta_l^2} \tag{10}$$

where A_μ is an appropriate normalization constant and $\zeta_l = (R_{QM,l} - R_{QM,l}^0)/s_l$. The parameter s_l defines the standard deviation of the lth one-dimensional Gaussian function, $\phi_0(\zeta_l)$, to be $s_l/\sqrt{2}$ (Figure 1) and, in turn, defines the Gaussian envelope width for a given multiwavelet primitive, $\phi_{\mu,\sigma,\delta}(\zeta_l)$, to be $s_l/(\sqrt{2}a^\sigma)$. Thus, s_l determines the degree of overlap between multiwavelet primitives and is expected to affect basis set completeness and singularity of an overlap matrix constructed from these primitives. The corresponding free propagated form is exactly given by[2,39,45]

$$\phi_{\mu,\sigma,\delta}(\zeta_l, t) = e^{-i\hat{K}t}\phi_\mu\left(a^\sigma\zeta_l + b\left(\delta + \frac{1}{2}\right)\right)$$

$$= \frac{1}{[\sqrt{2}\,s_l(t)]^{\mu+1/2}}\phi_\mu\left(\frac{a^\sigma\zeta_l + b(\delta + 1/2)}{\sqrt{2}\,s_l(t)}\right) \tag{11}$$

where $s_l(t) \equiv [\,{}^1\!/_2 + ita^{2\sigma}/(ms_l^2)]^{1/2}$ and $\hat{K} = -[1/(2m)](\partial^2/\partial R_{QM,l}^2) = -\{1/[(2ms_l^2)]\}(\partial^2/\partial\zeta_l^2)$ is the one-dimensional kinetic energy operator for a particle of mass m. Unpropagated and propagated multiwavelets are shown in Figure 3. One should note that as $t \to 0$, the width of the wavelet primitive, $\varphi_{\mu,\sigma,\delta}$, along $R_{QM,l}$, approaches $s_l/(\sqrt{2}a^\sigma) > 0$. Thus, the sign problem that is associated with Fourier propagation approaches, including the Feynman path integral approach, may be circumvented.

B. Construction of $\{\phi_{l,k_l}\}$ from $\{\phi_{\mu,\sigma,\delta}\}$. We note that the structure described above can produce a set of multiwavelets that is numerically overcomplete in the space that it spans. This poses a problem in the multiconfigurational limit discussed in the previous section. In this situation, one can calculate the orthonormal one-dimensional single particle basis functions, $\phi_{l,k_l}^{[j]}$, of eqs 4 and 5. Toward this, we first compute the principal components of the multiwavelet overlap matrix:

$$S_l(\delta,\sigma,\mu; \delta',\sigma',\mu') \equiv \int d\zeta_l \phi_{\mu,\sigma,\delta}^*(\zeta_l)\phi_{\mu',\sigma',\delta'}(\zeta_l) \tag{12}$$

through singular value decomposition (SVD),[70,71]

$$U^TSV = \Sigma \tag{13}$$

where U and V^T are orthogonal matrices and Σ is a diagonal singular value matrix. The matrices U and V^T, in general, form a biorthogonal basis, but since S is a symmetric square matrix, $V = U$. The columns of the matrix V provide a rotation from the basis of multiwavelets to the orthonormal one-dimensional single particle basis functions of eqs 4 and 5. One could represent $\phi_{l,k_l}^{[j]}$ in this new basis, as

$$\phi_{l,k_l}(\zeta_l) = \frac{1}{\sqrt{\Sigma_{k_l}}} \sum_{\mu=0}^{\mu_{max}-1} \sum_{\sigma=0}^{\sigma_{max}} \sum_{\delta=0}^{a^\sigma-1} V_{\mu,\sigma,\delta;l}^{(k_l)}\phi_{\mu,\sigma,\delta}(\zeta_l) \tag{14}$$

where the singular values, Σ_{k_l}, serve to normalize the ϕ_{l,k_l} to unity. The singular value for a given singular vector determines the significance of that principal component in constructing the multiwavelet overlap matrix. Hence, a truncated basis with invertible overlap can be constructed by retaining only the vectors with non-negligible singular values.

It is useful to consider the symmetry introduced by translation and scaling together with the localization of translates (Figure 1) in constructing the overlap matrix in eq 12. This leads to significant data compression and reduction in computational scaling. Figure 4 illustrates the high degree of symmetry in the multiwavelet overlap matrix (eq 12), as well as the use of these symmetries, together with sparsity, when carrying out a matrix vector multiplication. Thus, these properties reduce computational cost in general wherever the multiwavelet basis is implemented. This includes the construction of the total Hamiltonian, to be discussed in later sections. A detailed examination of scaling associated with the multiwavelet overlap is provided in the Supporting Information.

In practice, the number of principal components retained (N_{basis}) is determined by a singularity threshold δ_{SVD} as follows. Let all of the singular values, $\{\Sigma_{k_l}\}$, be ordered from smallest ($k_l = 1$) to largest ($k_l = N_p$), where N_p is the total number of wavelet primitives,

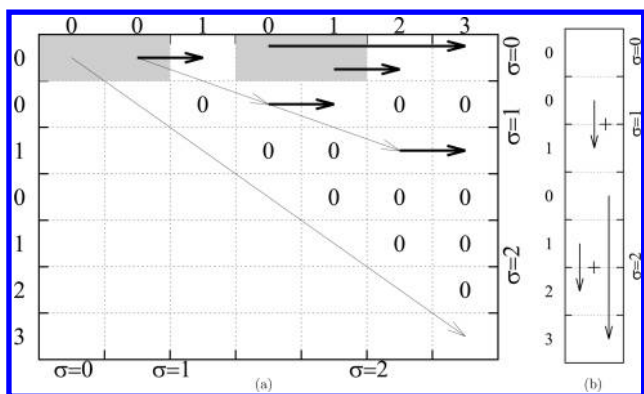$$N_p = \mu_{max}\sum_{\sigma=0}^{\sigma_{max}} a^\sigma = \mu_{max}\frac{a^{\sigma_{max}+1} - 1}{a - 1} \tag{15}$$

Figure 4. (a) Sketch representing the structure of the overlap matrix. The numbers along the axes represent the values for the translate, δ, where the scales (or wavelet generations) are represented using the corresponding σ values noted. The gray boxes indicate the regions that need to be calculated. Boxes that are connected by thin arrows are related by scaling relations which reduce the computational overhead. Boxes connected by thick arrows are identical. As noted by the number of zeroes, the matrix is sparse. Since the matrix is symmetric, only the structure for the upper triangle is presented. (b) Sketch representing the reduction in computational overhead when the multiwavelet overlap matrix acts on a vector. For simplicity, the action of the first row block from panel (a) is shown to act on a corresponding vector and the associated operations are depicted in panel (b). Essentially, bceause of the relations between blocks 2 and 3 in the first row of panel (b), the corresponding matrix-vector operations can be simplified by replacing multiplications with additions as noted in panel (b). This is similar to the case for blocks 4−7 in the first row of panel (a), where the connections between blocks 4−7 and 5−6 are exploited in panel (b) again by replacing multiplications with additions. Clearly, further gains in computational effort are possible beyond the first row as a result of sparsity and symmetry.

Then, all singular vectors up to the largest corresponding value of f for which

$$\sqrt{\sum_{k_l=1}^{f} \Sigma_{k_l}^2} \leq \delta_{\mathrm{SVD}}$$

(16)

are excluded. The number of nonzero singular values, $N_{\mathrm{basis}} = N_p - f$, i.e., the dimension of Σ, determines the number of principal components that compose the multiwavelet basis.

C. Representation of the Hamiltonian in the Multiwavelet/Diabatic State Basis.

1. Nuclear Kinetic Energy Operator.
The nuclear kinetic energy portion may be written as a tensor product of one-dimensional kinetic energy representations:

$$K_{k_l,k_l}^{(l)} = -\frac{1}{2m} \langle \phi_{l,k_l} | \hat{K}^{(l)} | \phi_{l,k_l} \rangle$$

$$= -\frac{1}{2ms_l^2} \sum_{\mu,\mu'} \sum_{\sigma,\sigma'} \sum_{\delta,\delta'} a^{\sigma+\sigma'} V_{\mu,\sigma,\delta;l}^{(k_l)*} V_{\mu',\sigma',\delta';l}^{(k_l)}$$

$$\times \langle \phi_{\mu+1,\sigma,\delta\cdot} | \phi_{\mu'+1,\sigma',\delta_{l'}} \rangle$$

(17)

that is,

$$\langle \Upsilon_{k'} | [\sum_l \hat{K}^{(l)}] | \Upsilon_k \rangle = \sum_{l=1}^{d} (\mathbf{1}^{(N_{<l})} \otimes \mathbf{K}^{(l)} \otimes \mathbf{1}^{(N_{>l})})$$

$$= \sum_{l=1}^{d} \mathcal{P}(\bar{N}, N_{<l}N_{\mathrm{SVD},l}) (\mathbf{1}^{(N_{<l}N_{>l})} \otimes \mathbf{K}^{(l)}) \mathcal{P}(\bar{N}, N_{>l})$$

(18)

where the quantity $\mathbf{K}^{(l)}$ is the matrix composed of terms given in eq 17. In addition, we have extended to multiple dimensions using a Kronecker tensor product[72] over all degrees of freedom. The Kronecker tensor product between an $M_A \times N_A$ matrix ($\mathbf{A}$) and an $M_B \times N_B$ matrix ($\mathbf{B}$) is an $M_A M_B \times N_A N_B$ matrix with elements, $[\mathbf{A} \otimes \mathbf{B}]_{(M_B^{i+k}, N_B^{j+l})} = A_{ij} B_{kl}$. The quantity $\mathbf{1}^{(N)}$ represents the $N \times N$ identity matrix and $N_{<l}$ ($N_{>l}$) is the scalar product of basis set sizes, $N_{\mathrm{basis},l'}$ for all degrees of freedom, l', less (greater) than l. For example,

$$N_{<l} = \prod_{l'=1}^{l-1} N_{\mathrm{SVD},l'}$$

(19)

The quantity $\bar{N}$ ($= \Pi_{l'=1}^{d} N_{\mathrm{SVD},l'}$), represents the total number of rows or columns in $\mathbf{K}$. The stride permutation, $\mathcal{P}(N, M)$,[72] is an operator that acts on a vector of length N, producing a new vector of identical length with rearranged elements with a stride of length M. The stride permutation that acts on a vector of N elements with stride M is to be interpreted as a transpose operation acting on a matrix of size $(M \times N/M)$. For example, the permutation that acts on a vector of length $N = 6$ with stride M = 2 is

$$\mathcal{P}(6, 2) \begin{pmatrix} v_1 \\ v_2 \\ v_3 \\ v_4 \\ v_5 \\ v_6 \end{pmatrix} = \begin{pmatrix} v_1 \\ v_3 \\ v_5 \\ v_2 \\ v_4 \\ v_6 \end{pmatrix}$$

(20)

We note that the term $(\mathbf{1}^{(N_{<l}N_{>l})} \otimes \mathbf{K}^{(l)})$ in the second line in eq 18 represents a block diagonal matrix. Thus, its multiplication to a vector can be easily parallelized by sending each individual block multiplication to a separate node. The stride permutations may readily be affected by transpose operations.[72]

2. Potential Energy Operator.
We remind the reader that the electronic potential surface is constructed "on-the-fly" in QWAIMD. Specifically, in MC-QWAIMD, which is the method used here, the potential surface is constructed in the diabatic state representation. Details of the methodology can be found in refs 4 and 7. Here, only a summary is provided, as is pertinent to the current discussion.

The adiabatic electronic structure, $\Psi_{el}^{(n)}$, is written as a multiconfigurational expansion[6,7,73−81] of local, single particle state functions, $\{\chi_I^{(diab)}\}$, as

$$\Psi_{el}^{(n)}(\mathbf{r}_{el}, \mathbf{R}_{\mathrm{QM}}, \mathbf{R}_C; t) = \sum_I c_I^{(n)}(\mathbf{R}_{\mathrm{QM}}, \mathbf{R}_C; t) \chi_I^{(diab)}(\mathbf{R}_C, \mathbf{r}_{el}; t)$$

(21)

The quantities $\mathbf{R}_{\mathrm{QM}}$, $\mathbf{R}_C$, and $\mathbf{r}_{el}$ are the quantized nuclear coordinates, the classically treated nuclear degrees of freedom, and electronic coordinates, respectively. As noted, the coefficients $c_I^{(n)}$ depend on both $\mathbf{R}_{\mathrm{QM}}$ and $\mathbf{R}_C$. The state functions, $\{\chi_I^{(diab)}\}$, depend parametrically on $\mathbf{R}_C$ and are chosen to have no explicit dependence on the quantum nuclear degrees of freedom. In this sense, $\{\chi_I^{(diab)}\}$, may be interpreted as diabatic functions:[82−89] and $\langle \Phi_I^{(diab)} | \nabla_{\mathbf{R}_{\mathrm{QM}}} | \Phi_J^{(diab)} \rangle = 0$. The state functions $\{\chi_I^{(diab)}\}$ are propagated in time through an extended Lagrangian formalism[7] and the associated time-dependent states are used within a nonorthogonal CI formalism to compute, "on-the-fly" the quantum nuclear potential surface. (The electronic structure is time-dependent because of the fact

that QWAIMD is a quantum-classical formalism, where the dynamics of the classical nuclei, influences the electronic structure and hence the potential on the quantum nuclei.) This computational methodology shows improved scaling through the following steps:

(a) The diabatic approximation for these states is further strengthened by eliminating the quantum nuclear position dependence of the electronic basis. Instead adaptive-mesh based Gaussian electronic basis functions are introduced and these encompass the quantum nuclear grid region. This allows great simplification in computing the "on-the-fly", quantum-grid dependent nonorthogonal configurational interaction formalism (with negligible loss in accuracy), where the CI-matrix elements are easily calculated through reuse of two-electron integrals as a result of the diabatic approximation.

(b) At the initial time step, the diabatic states are located using a Shannon entropy-based sampling function that facilitates the creation of localized electronic structure groups.

(c) The diabatic states are computed on an adaptive mesh that is determined using a technique that is similar to the h-type mesh refinement procedure known in computational fluid dynamics.[26]

Details of this computational methodology can be obtained from refs 4, 6, and 7.

One of the biproducts of this methodology is that electronic energies are available within the diabatic and adiabatic representations. In this publication, only the adiabatic representation is used. Given adiabatic or diabatic energies: $\{\varepsilon_i(\mathbf{R}_{QM})\}$, representation within the multiwavelet basis is given by the matrix elements,

$$\langle \Upsilon_{k'}|\varepsilon_0|\Upsilon_k\rangle \equiv \int d\mathbf{R}_{QM}\, \Upsilon_{k'}^*(\mathbf{R}_{QM})\varepsilon_0(\mathbf{R}_{QM})\Upsilon_k(\mathbf{R}_{QM}) \tag{22}$$

where the basis functions are as defined above.

D. Propagation of the Quantum Nuclear Wavepacket in the Multiwavelet Basis. The propagator, $\exp[-i\hat{H}t/\hbar]$, can be expressed in terms of the Bessel–Chebychev expansion derived from the Jacobi–Anger formula,[90]

$$\exp(-\imath zx) = \sum_{n=0}^{\infty}(2 - \delta_{n,0})(-i)^n J_n(z)T_n(x) \tag{23}$$

which has commonly been used in quantum dynamics.[91–94] Hence,

$$\exp(-i\hat{H}t/\hbar) = \exp(-i\overline{\overline{H}}t/\hbar)\sum_{n=0}^{\infty}(2-\delta_{n,0})(-i)^n$$
$$\times J_n(t\cdot\Delta\hat{H}/\hbar)T_n(\hat{H}_{norm}) \tag{24}$$

where $\hat{H}_{norm}$ is the normalized electronic Hamiltonian matrix: $\hat{H}_{norm} = (\hat{H} - \overline{\overline{H}})/\Delta\hat{H}$, with $\overline{\overline{H}} = {}^1\!/_2(\hat{H}_{max} + \hat{H}_{min})$, and $\Delta\hat{H} = {}^1\!/_2(\hat{H}_{max} - \hat{H}_{min})$. The quantities $\hat{H}_{max}$ ($\hat{H}_{min}$) are the maximum (minimum) eigenvalues of the truncated, finite matrix approximation to the vibrational Hamiltonian matrix, and for real matrices, are obtained from Gerschgorin's disk theorem.[95,96105] The quantities $(T_n(x) \equiv \cos(n\cos^{-1} x))$ are the Chebychev polynomials of the first type and $J_n(z)$ are the cylindrical Bessel functions. Specifically, the Chebychev expansions for the normalized form of the matrix, $\hat{H}$, are generated by the recursion relation,[97]

$$T_n(\hat{H}_{norm}) = 2\hat{H}_{norm}T_{n-1}(\hat{H}_{norm}) - T_{n-2}(\hat{H}_{norm}) \tag{25}$$

where $T_0(\hat{H}_{norm}) = 1$ and $T_1(\hat{H}_{norm}) = \hat{H}_{norm}$. For all expressions above, $\hat{H}$ is represented using eqs 17, 18, and 22.

V. SELECTION OF SUITABLY ACCURATE, STABLE, AND COMPACT MULTIWAVELET STRUCTURES TO DEPICT THE VIBRATIONAL WAVEPACKET

We now investigate two fundamental aspects of basis set construction, namely, information compression and accuracy. These two conflicting facets of a basis are reflected in the following parameters: basis set size, as defined by both the number of wavelet primitives, N_p, and singular components, N_{basis} ($\leq N_p$); the zeroeth generation ($\sigma = 0$) Gaussian scaling factor s_l, as defined in Figure 1 and in the discussion following eq 10; and the singular threshold, δ_{SVD}, as defined by eq 16. Here, we characterize the role of these parameters in determining a suitable multiwavelet basis set and justify our choices of $s_l/\sqrt{2} = L/6$, where L is the length of the integration domain interval (Figure 1) and $\delta_{SVD} = 1.0 \times 10^{-6}$. We furthermore demonstrate that required accuracies for treatment of vibrational dynamics may be achieved for basis set sizes N_p, $N_{basis} \approx 20–30$, 3–5 times lower than the size of a typical grid basis used in QWAIMD. While the discussion here is one-dimensional, the parameters chosen extend to high dimensions and are used later in the publication to construct the full wavepacket for a shared proton in a hydrogen-bonded system. The interplay between these parameters may be considered in the following ways:

(a) **Basis set compression:** The ability of a basis set to compress the physical information content of a quantum vibrational wavepacket is manifest in its ability to span the Hilbert space of the wavepacket with as small a number of components as possible. Thus, a small (low N_p) wavelet primitive set with high redundancy ($N_{basis} \ll N_p$) may be desired for this purpose. This suggests a preference toward higher values of δ_{SVD} and s_l. In addition, for multiwavelets, however, compression enters into the basis in its ability to introduce sparseness in computed matrices at the wavelet primitive level. This is achieved by limiting the degree of overlap between neighboring translates, indicating a preference toward lower values of s_l, thus potentially placing a limit on attainable redundancy. Furthermore, a lower value of s_l may be preferable in that it increases the span of the basis in momentum space by compression of the wavelet's spatial extent. Alternately, a larger value for s_l, combined with a larger σ_{max}, allows for a larger spread and filtering in the momentum representation.

(b) **Accuracy:** The requirement that a basis set faithfully reproduce the physics of a quantum vibrational problem will, of course, place lower limits on N_p and N_{basis}. Furthermore, it places bounds on s_l. Excessively large values of s_l can lead to greater delocalization of the basis functions and reduced span in momentum space, requiring compensation with higher N_p (and associated σ_{max}). However, a choice of s_l that is excessively small can under-represent the tails and spatial regions between translates (Figure 1). Similar bounds exist for δ_{SVD}. On the one hand, lower values of δ_{SVD} can increase basis set span by including more principal components. The penalty here is that such lower singularity cutoffs bring the wavelet primitive overlap closer to divergence in its inverse and, thus, reduce attainable numerical stability. Conversely, higher cutoffs will sacrifice span for stability.

Given these restrictions, a numerical analysis of the interplay between these parameters is now presented.
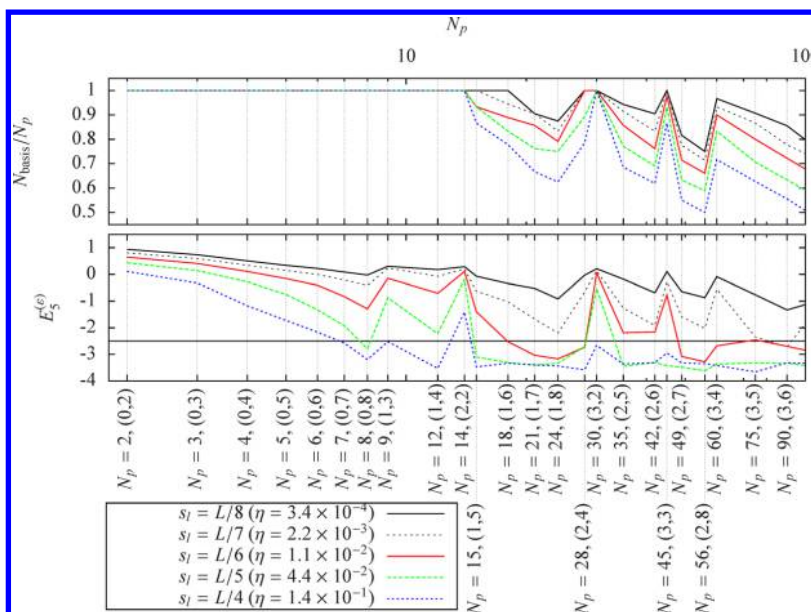
Figure 5. (top) Fraction of principal components retained, N_{basis}/N_p, versus number of wavelet primitives, N_p for several values of s_l/L at $\delta_{SVD} = 10^{-6}$. (bottom) Basis set accuracy vs N_p as characterized by eq 27 for analytical free particle under Neumann boundary conditions ($E_n = \alpha n^2$, where $\alpha = 1.852$ mHa ≈ 1.162 kcal/mol; $L = 1.200$ bohr; $N = 5$). Horizontal line at $E_5^{(\varepsilon)} = -2.5$, corresponds to a relative error in eigenenergies of $\sim 2 \times 10^{-3}$. For multiple basis sets with identical N_p, the basis with the lowest value of $E_5^{(\varepsilon)}$ is plotted. In the abscissa, the truncated wavelet primitive sets are also labeled according to maximum scale and Hermite order, $(\sigma_{max}, \mu_{max})$. The legend also includes values of η, as defined by eq 26.

To characterize compression, we will investigate the dependence of N_{basis}/N_p on s_l and δ_{SVD}. Furthermore, the potential to introduce sparsity is characterized by the height of the Gaussian envelope at the domain edge relative to its height at the center,

$$\eta = \frac{\phi_{\mu=0}(L/2)}{\phi_{\mu=0}(0)} \qquad \forall \; \sigma \tag{26}$$

a measure that also characterizes the overlap between neighboring translates. The dependence of basis set accuracy on N_p will also be characterized for different values of s_l and δ_{SVD} to benchmark the effect of multiwavelet compression on accuracy.

To characterize the performance of a given basis set, we define measures of error in reproducing a given subset of eigenenergies. Given that error in an eigenenergy can increase in proportion to the magnitude of an eigenvalue itself, an order of magnitude measure for the *relative* eigenenergy error is defined,

$$E_N^{(\varepsilon)}(\sigma_{max}, \mu_{max}) \equiv \left\langle \log_{10} \left(\left| \frac{\varepsilon_n^{(QM)} - \varepsilon_n^{(anal)}}{\varepsilon_n^{(anal)}} \right| \right) \right\rangle_{0 \le n < \min(N_{basis}, N)} \tag{27}$$

where $\varepsilon_n^{(QM)}$ is the computed eigenenergy, $\varepsilon_n^{(anal)}$ is the analytical eigenenergy (or eigenenergy obtained from the grid calculation), and N is the total number of eigenstates considered in the analysis. Thus, eq 27 amounts to a geometric mean of the relative errors in the N eigenenergies included. The angle brackets represent an average over all computed eigenstates with quantum numbers n up to $\min(N_{basis}, N)$, given that the number of computed eigenstates is limited by the number of principal components and can vary with basis set.

Accuracy is benchmarked for the first few eigenfunctions of (a) the free particle system obeying Neumann[98] boundary

conditions, (b) the quantum Harmonic oscillator, and (c) a set of 80 configurations of the ClHCl− bihalide cluster, which were independently obtained from an MC-QWAIMD simulation.[7] While the results in all cases are similar, here, we highlight the results from the free particle case because (i) we find this to be numerically the most challenging, and (ii) the analytical result from Feynman path integration[45] is one that involves rapidly oscillatory functions, where the oscillation frequency essentially increases as the Feynman paths connect points in configuration space that are farther and farther apart. (On this particular aspect, see ref 38 for a filtered representation for paths with well-separated end points, that does not suffer from the well-known quantum dynamical sign problem. The "distributed approximating functional" propagator used in ref 38 is also formed from Hermite functions, which is a feature in common with the multiwavelets presented here.) The motivation for gauging accuracy by comparing against the free particle eigenfunctions under Neumann boundary conditions arises from this system's ability to characterize the variational minimization of the Hamiltonian with respect to uniform spatial and spectral completeness of the multiwavelet basis. The ground-state Neumann eigenfunction is a constant and characterizes completeness at all grid points uniformly. Furthermore, inclusion of excited states with the ground state provides a similar benchmark of basis set fidelity over kinetic energy ranges within which a quantum wavepacket can reside. Benchmarks for the harmonic oscillator analytical test case and set of 80 configurations of the ClHCl− bihalide cluster are presented in the Supporting Information.

The quantity N in eq 27 is chosen to include all eigenstates inside a 30 mHa ($\sim$18.83 kcal/mol) cutoff. This upper limit corresponds to probing energies that are an order of magnitude greater than $k_B T$ ($\sim$0.6 kcal/mol) at room temperature and provides an adequate margin for describing many realistic systems. Under this constraint, N will be small enough so that
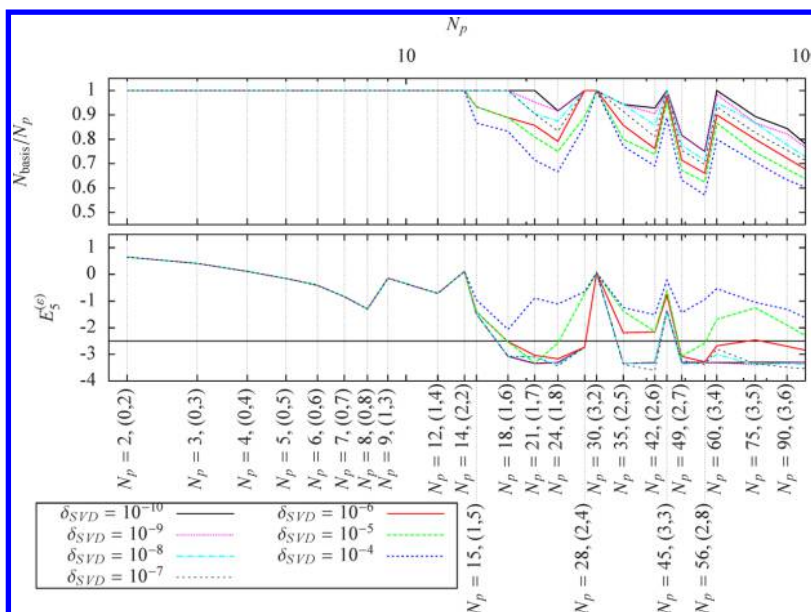
Figure 6. (Top) Fraction of principal components retained, N_{basis}/N_p, versus the number of wavelet primitives, N_p for several values of δ_{SVD} at $s_l/L =$ $L/6$. (Bottom) Basis set accuracy vs N_p as characterized by eq 27 for analytical free particle under Neumann boundary conditions ($E_n = \alpha n^2$, where α = 1.852 mHa ≈ 1.162 kcal/mol; L = 1.200 bohr; N = 5). Horizontal line at $E_S^{(\varepsilon)} = -2.5$ corresponds to a relative error in eigenenergies of ∼2 × 10^{-3}. For multiple basis sets with identical N_p, the basis with the lowest value of $E_S^{(\varepsilon)}$ is plotted. In the abscissa, the truncated wavelet primitive sets are also labeled according to maximum scale and Hermite order, (σ_{max}, μ_{max}).

only multiwavelet structures for which $\sigma_{max} \leq 3$ need to be considered.

The upper plot in Figure 5 presents a characterization of basis set redundancy (N_{basis}/N_p) as a function of N_p for several values of s_l/L at $\delta_{SVD} = 10^{-6}$. Removal of redundant principal components consistently begins with N_p = 15 for all values of s_l/L probed with as many as half of the redundant vectors being removed. This redundancy does not depend monotonically on N_p, but rather, exhibits monotonic increases with increasing σ_{max} and μ_{max} independently. Because both of these parameters are related to the span of momentum components (see Figure 2), this suggests that redundancy in the wavelet primitive space is largely caused by overcompleteness in momentum space introduced through a high μ_{max} at a given σ_{max}. This root of overcompleteness comes in addition to the expected trend of increased redundancy with increased s_l, which is a result of high spatial overlap between translates.

The lower plot in Figure 5 presents a characterization of basis set accuracy as a function of N_p for several values of s_l/L at $\delta_{SVD} = 10^{-6}$. To gauge accuracy, a horizontal line is drawn at $E_S^{(\varepsilon)} = -2.5$, which corresponds to a relative error in eigenenergies of ∼2 × 10^{-3}. Eigenenergies, for which the value is on the order of mHa, exhibit errors on the order of μHa, well within the range of accuracy for electronic structure methods. Thus, μHa accuracy is already attainable for multiwavelet sets with the number of elements (N_p) being ∼20−30 for $s_l = L/6, L/5, L/4$, as compared with typical grid basis sets of ∼100 elements used in grid-based QWAIMD propagation. Furthermore, this level of accuracy is not limited to one value of σ_{max}. This allows for some flexibility in choosing the level of "wavelet" character in a basis set. Accuracy is reduced substantially for values of $s_l < L/6$ but not for higher values, suggesting that the upper bound on frequency span for the multiwavelet basis is not exceeded by the highest eigenstate considered.

Figure 6 presents a characterization of basis set redundancy (N_{basis}/N_p) and accuracy as a function of N_p for several values of

δ_{SVD} at $s_l = L/6$. For the values of singularity threshold (δ_{SVD}) examined, basis set undercompleteness tends to be a larger source of error than numerical singularity, because higher thresholds give large relative errors while level of accuracy tends to plateau, if not decrease, for $\delta_{SVD} \leq 10^{-6}$, providing a significant level of flexibility with regard to the level of redundancy. This suggests that the eigenstates considered have negligibly small projections along the less numerically stable principal components added by reducing δ_{SVD} to the lowest values examined here. We emphasize that, as in the case of varying s_l, the same levels of accuracy may be found across different values of σ_{max}, thus, retaining a flexibility in choosing the degree of "wavelet" character in the basis.

Considering the criteria given above, the remainder of this work will focus on dynamical benchmarks with the (σ_{max}, μ_{max}) = (1,7) set of wavelet primitives at $s_l = L/6$ and $\delta_{SVD} = 10^{-6}$. This basis set has 21 wavelet primitives, or approximately one-fifth of the typical 100 grid points used in previous QWAIMD calculations. For $s_l = L/6$ and $\delta_{SVD} = 10^{-6}$, this set may be further compressed to 18 basis functions while retaining μHa accuracy at mHa eigenenergies. Of the choices probed here, $s_l = L/6$ gives the smallest overlap between translates (i.e., value of η) that retains this desired level of accuracy. If greater flexibility in spatial localization is desired, one may choose the (σ_{max}, μ_{max}) = (2,4) basis set instead, where N_p = 28 is still a reasonable compression, when compared to typical grid basis values (although all principal components are retained for this basis). Both basis sets give similar performance, in terms of accuracy.

VI. QUANTUM DYNAMICAL BENCHMARKS FOR THE ClHCl$^-$ BIHALIDE SYSTEM

Having benchmarked several multiwavelet structures above, we found that the (σ_{max}, μ_{max}) = (1,7) basis accurately represents the quantum energy levels relevant to room-temperature simulations, compared to the grid basis sets typically used in QWAIMD. We now benchmark the performance of this basis

set in simulation of the quantum dynamics for a one-dimensional (1D) and three-dimensional (3D) representation of the shared proton wavepacket in the ClHCl$^-$ bihalide system. As is the case with the other QWAIMD simulations, the shared proton is treated as a quantum wavepacket and all other nuclear degrees of freedom are treated classically, with forces computed using the time-dependent electronic structure. (See section IV(C2).) The electronic structure is calculated "on the fly" using the multireference diabatic state formalism with electronic state represented by eq 21. The simulations are carried out for a duration of 2 ps for all 1D cases and a duration of 1.5 ps for the 3D case.

The significance and challenge involved in simulating the ClHCl$^-$ system is important to note. This system contains a shared proton undergoing excursions along the Cl−Cl axis. The motion of the proton is (a) coupled to the two peripheral atoms, and (b) dictated by the highly anhammronic nature of the potential surface.[4,7] This makes the problem challenging, not only for the commonly utilized harmonic analysis constructed at optimized geometries but also many state-of-art methods such as the nuclear electronic orbital approach constructed at the MP2 level,[99] as well as the CC-VSCF-MP2[99−103] method. Previously, we showed that the vibrational density of states calculated from the TDDS implementation of adiabatic QWAIMD[4] is able to provide quantitative agreement with experimental results. Furthermore, the multiconfigurational generalization to QWAIMD[7] was benchmarked against results obtained from both adiabatic QWAIMD as well as from gas-phase spectroscopy experiments for several bihalide systems. In all of the previous work described here, the wavepacket for the shared quantum proton was represented with a discrete regular grid basis. Here, we build on the work in ref 7 by replacing this grid representation with an orthogonal basis derived from the multiwavelet structure, as described in section IV.

For the 1D case, diabatic state bases of five and nine diabatic states (i.e., $N_{DM} = 5, 9$, respectively in eq 21) are employed,[6,7] whereas for the 3D case, the shared proton potential is computed within a 9-diabatic-state level of theory. The electronic structure is computed using a hybrid atom-centered Gaussian basis localized on the classical nuclei, and a basis of Gaussians localized on specially chosen grid points that span the quantum nuclear subspace.[7] In this case, the basis functions localized on the Cl atoms is the 6-31G+(d,p) atom-centered basis set, with sto-3G basis functions floating on a grid encompassing the quantum nuclear degrees of freedom.[7] This choice has been shown to have accuracy comparable to atom-centered aug-cc-pvtz basis functions (see Table 2 in ref 9). All of these functions adapt to the position of the classical nuclei, as the dynamics evolves. All the calculations are performed using locally built modifications to a development version of the Gaussian series of electronic structure programs.

The initial structures for dynamics are obtained from a geometry optimization at B3LYP/6-31+G(d,p) level of theory. The initial shared proton wavepacket is a superposition of eigenstates $\psi_n(\mathbf{R}_{QM}; R_C(0))$ of the Hamiltonian as defined in sections IV(C1) and IV(C2),

$$\Psi_0^{(QM)}(\mathbf{R}_{QM}; t = 0) = \sum_n b_n \psi_n(\mathbf{R}_{QM}) \tag{28}$$

For the 1D case, the wavepacket is initially set to the ground state,

$$b_n = \begin{cases} 1 & n = 0 \\ 0 & n > 0 \end{cases} \tag{29}$$

or to a Boltzmann-weighted thermal superposition,

$$b_n = \sqrt{\frac{1}{Z_C} \exp\left(-\frac{\varepsilon_n - \varepsilon_0}{k_B T_0}\right)} \tag{30}$$

where $\{\varepsilon_n\}$ are the eigenenergies associated with the eigenfunctions, $\{\psi_n\}$ and the canonical partition function, Z_C normalizes the coefficients b_n. For the thermal initial states, $T_0 = 300$ K. Dynamical simulation within the 3D representation of the shared proton, starts from a ground-state initial wavepacket, defined by eqs 28 and 29.

As noted earlier, the simulations are carried out for a duration of 2 ps for all 1D cases and a duration of 1.5 ps for the 3D case. In all cases, the total energy was well-conserved with a standard deviation in total energy on the order of 0.05 kcal/mol. Furthermore, deviations between the multiwavelet representation and grid representation are minimal as noted in Table 1. Table 1 summarizes the comparisons of total energies, the expectation value of the wavepacket flux:

$$\mathbf{J}(t) = \Re\left[\left\langle \Psi_j^{(QM)}(t) \left| \frac{-\iota\hbar}{m} \nabla \right| \Psi_j^{(QM)}(t) \right\rangle\right] \tag{31}$$

$$\mathbf{J}(\omega) = \lim_{T \to \infty} \int_{t=0}^{t=T} dt \, e^{(-i\omega t)} \left\{ \Re\left[\left\langle \Psi_j^{(QM)}(t) \left| \frac{-i\hbar}{m} \nabla \right| \Psi_j^{(QM)}(t) \right\rangle\right]\right\} \tag{32}$$

and the donor−acceptor distance. (The quantity $\Psi_j^{(QM)}(t)$ is as defined in eq 4. The dependence on $\mathbf{R}_{QM}$ has been dropped on account of the bracket.) The degree of fluctuation in any such observable, $O(t)$, is measured by its standard deviation, $\sigma[O]$, over the time interval of simulation. Thus, for consistency, the deviation between an observable in a multiwavelet based simulation, $O_{wav}(t)$, and its counterpart in a grid-based simulation, $O_{DAF}(t)$ is given by the root-mean-square of the difference between these observables per time step,

$$\Delta[O] \equiv \sqrt{\frac{\sum_i (O_{wav}(t_i) - O_{DAF}(t_i))^2}{N}} \tag{33}$$

where N is the total number of quantum propagation time steps. The total energies as a function of time exhibit agreement of order 10^{-5} kcal/mol between the multiwavelet and grid-based propagation schemes over a simulation duration of 2 ps. Both schemes exhibit similar energy conservation properties (0.05 kcal/mol) and the Cl−Cl stretch shows relative errors between the two propagation schemes of <10%, while the shared proton flux tends to deviate by as much as 25% between the two propagation schemes.

A. Analysis of the Quantum Nuclear Eigenstates as a Function of Time. In this section, we probe the behavior of eigenstates and potential. We specifically perform this analysis for two different simulations. One of these simulations uses nine diabatic states, whereas the other uses five. For a detailed discussion of the performance of the five- and nine-diabatic state potentials in faithfully representing the electronic structure of the ClHCl$^-$ bihalide structure, the reader is referred to ref 7. However, these two cases represent qualitatively different physics, since a small number of diabatic states generally result in a relatively confined potential surface to yield higher vibrational frequencies, as already noted in ref 7. We use this
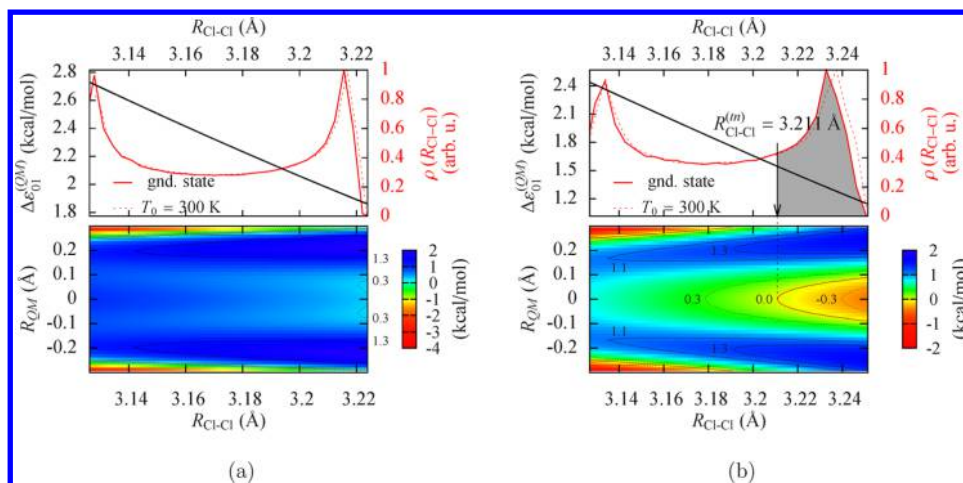
Figure 7. Instantaneous eigenenergy analysis for a 2 ps dynamics duration simulation using the $(\sigma_{max}, \mu_{max}) = (1,7)$ basis. (Top) Red curves: radial distribution function, $\rho(R_{Cl-Cl})$, of donor−acceptor distances for (a) five diabatic states (eq 21 with $N_{DB} = 5$) and (b) nine diabatic states (eq 21 with $N_{DB} = 9$). The area under $\rho(R_{Cl-Cl})$ (shaded in gray) indicates the donor−acceptor configurations, for which the zero point energy of the quantum proton drops below the intermediate barrier height ($\sim 35\%$ and 36% of the total area under $\rho(R_{Cl-Cl})$ for the ground state (see eqs 28 and 29) and thermal (see eqs 28 and 30) initial wave functions, respectively for the nine-density matrix case, and zero for the five-density matrix case). The stretch distance $R_{Cl-Cl} = 3.211$ Å corresponds to the donor−acceptor configuration for which the zero point energy equals the barrier height for the shared proton. Black curve: $0 \leftarrow 1$ transition energy for shared proton. (Bottom) Contour map of the difference between the zero point energy and potential energy surface for the shared proton with position coordinate R_{QM} (vertical axis). The contours at 0.0 kcal/mol correspond to the classical turning points and negative energies correspond to the region where the shared proton zero point energy drops below the potential energy surface.
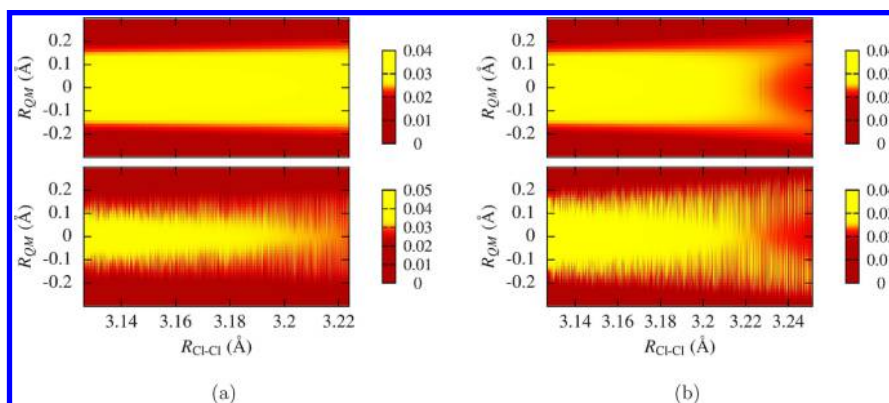

Figure 8. Wavepacket probability densities for a 2 ps dynamics duration simulation using the $(\sigma_{max}, \mu_{max}) = (1,7)$ basis starting from (top panels) an initial ground state condition (eqs 28 and 29) for (a) five diabatic states (eq 21 with $N_{DB} = 5$) and (b) nine diabatic states (eq 21 with $N_{DB} = 9$). Bottom panels show initial thermal superposition (eq 28 and 30 with $T_0 = 300$ K) for (a) five diabatic states (eq 21 with $N_{DB} = 5$) and (b) nine diabatic states (eq 21 with $N_{DB} = 9$).

difference to further probe the behavior of eigenstates and potential surface. An instantaneous eigenstate decomposition is used to characterize the properties of the shared proton's quantum wavepacket for the adiabatic ground electronic state,

$$\Psi_0^{(QM)}(\mathbf{R_{QM}}; t) = \sum_n b_n(t)\psi_n(\mathbf{R_{QM}}; R_C(t)) \tag{34}$$

The basis functions $\psi_n(\mathbf{R_{QM}}; R_C(t))$ diagonalize the quantum nuclear Hamiltonian independently at every time step, t,

$$\hat{H}(\mathbf{R_{QM}}; R_C(t))\psi_n(\mathbf{R_{QM}}; R_C(t)) = \varepsilon_n^{(QM)}(R_C(t))\psi_n(\mathbf{R_{QM}}; R_C(t)) \tag{35}$$

The notation in the above equations is meant to imply that the time dependence in the potential surface comes exclusively from the classical subsystem. For such systems, the instantaneous eigenstates are directly mapped onto eigenstates parametrically dependent on $\{\mathbf{R_C}\}$. We emphasize that the initial conditions defined by eqs 28−30 are special cases of this

instantaneous diagonalization associated with the simulation starting time, $t = 0$ ($b_n = b_n(t = 0)$, $\varepsilon_n = \varepsilon_n^{(QM)}(R_C(t = 0))$ and $\psi_n(\mathbf{R_{QM}}) = \psi_n(\mathbf{R_{QM}}; R_C(t = 0))$).

The bottom panels in Figure 7 gives the difference between the zero-point energy and the potential energy surface, $\varepsilon_0^{(QM)}(R_{Cl-Cl}) - V_{ClHCl^-}(R_{QM}; R_{Cl-Cl})$, as a function of quantum proton coordinate, R_{QM} and donor−acceptor distance, R_{Cl-Cl}. Regions where this quantity is negative correspond to "tunneling" domains where the zero point energy of the shared proton falls below the barrier energy. For the five-diabatic-state case, this does not occur during the course of the simulation. However, for the nine-diabatic-state case, an integral of the radial distribution function, $\rho(R_{Cl-Cl})$, starting at the configuration ($R_{Cl-Cl}^{(tn)} = 3.211$ Å), where the shared-proton zero-point energy is equal to the barrier height energy,

Table 2. Symmetric (ν_1) and Antisymmetric (ν_3) Vibrational Stretch Frequencies and Kinetic Energy Contributions from the Shared Proton ($\langle \hat{K}^{(1)} \rangle$) and the Cl Moieties ($K_{\{Cl\}}$) for the ClHCl$^-$ Bihalide Cluster for Multiwavelet (σ_{max}, μ_{max}) = (1,7) and Grid-Based Shared Proton Propagation Algorithms

	N_{DM}[a]	prop. scheme	ν_1[b] (cm^{-1})	ν_3[b] (cm^{-1})	$\langle \hat{K}^{(1)} \rangle$[c] (K)	$K_{\{Cl\}}$[c] (K)
1D	5[d]	multiwavelet	317 ± 8	800 ± 8,[f] 808[g]	347 (21)	41 (28)
	5[d]	grid	317 ± 8	800 ± 8[f]	347 (21)	42 (29)
	5[e]	multiwavelet	317 ± 8	800 ± 8,[f] 806[g]	359 (22)	42 (29)
	5[e]	grid	317 ± 8	800 ± 8[f]	359 (22)	43 (30)
	9[d]	multiwavelet	283 ± 8	634 ± 8,[f] 634[g]	286 (27)	47 (34)
	9[d]	grid	283 ± 8	634 ± 8[f]	287 (28)	50 (35)
	9[e]	multiwavelet	283 ± 8	617 ± 8,[f] 631[g]	301 (29)	48 (35)
	9[e]	grid	283 ± 8	617 ± 8[f]	301 (30)	51 (37)
3D	9[d]	multiwavelet	318 ± 11	785 ± 11[f]	3297 (65)	75 (53)
	9[d]	grid	318 ± 11	785 ± 11[f]	3302 (66)	78 (55)

[a]Defined in eq 21. [b]Denoted as $\nu \pm \delta\nu$, where ν is the peak position and $\delta\nu$ is the frequency uncertainty as determined by the time duration of the simulation. [c]Denoted as $\bar{K}$ ($\sigma[K]$), where $\bar{K}$ is the time average and $\sigma[K]$ is the standard deviation of K over the simulation duration. [d]Ground-state initial wave function (see eqs 28 and 29). [e]Thermal initial wave function (see eqs 28 and 30 with $T_0 = 300$ K). [f]Calculated from quantum flux (see eq 37). [g]Radial distribution function averaged $0 \to 1$ transition energy calculated using eq 38.

$$P^{(tn)} \equiv \int_{R_{Cl-Cl}^{(tn)}}^{\infty} dR_{Cl-Cl} \, \rho(R_{Cl-Cl}) \tag{36}$$

as illustrated by the shaded area in the top plot of Figure 7b, reveals that the zero point energy drops below the barrier height energy over ~35% and 36% of the trajectory for ground and thermal initial conditions, respectively. This difference is reinforced from the plot of shared proton wavepacket density (Figure 8) where the wavepackets exhibit qualitatively different shapes, particularly in the region of highest Cl−Cl stretch. The differing initial conditions (ground state versus thermal) do not qualitatively alter this discrepancy, contributing a slight aggregate increase in Cl−Cl stretch, as seen from both the radial distribution functions in the top panes of Figure 7 and increased antisymmetric oscillations in wavepacket density for the thermal initial case, as opposed to the initial ground state case in Figure 8. Finally, the morphology of the diabatic state potential is very different for five and nine diabatic states, and these aspects are consistent with those noted in ref 7, where it was shown that reducing the number of diabatic states increases quantum confinement.

B. Vibrational Properties for ClHCl$^-$: Interpretations Using an Adiabatic Dressed State Quantum Dynamics Model. We now compute the asymmetric stretch frequencies for the shared proton in two different ways. First, the frequency is directly obtained from the expectation value of the shared proton quantum flux correlation:

$$I_J(\omega) = \lim_{T \to \infty} \int_{t=0}^{t=T} dt \, e^{(-\iota\omega t)} \{ \langle \mathbf{J}(0) \cdot \mathbf{J}(t) \rangle_Q \} \tag{37}$$

where the expectation value of wavepacket flux is defined in eq 31. The term $\langle \cdots \rangle_Q$ represents the quantum ensemble average. That is, the ensemble average is constructed from the quantum dynamical portion of the trajectory. The quantity ω is the frequency. As seen from Table 2, the peak position of the asymmetric stretch fundamental derived from the spectrum given by eq 37 agrees well with the second approach, given by a shared proton ground to the first excited state ($0 \to 1$) transition energy averaged over the radial distribution function, $\rho(R_{Cl-Cl})$, of donor−acceptor distances,

$$\nu_3 \approx \int dR_{Cl-Cl} \, \rho(R_{Cl-Cl}) \varepsilon_{01}^{(QM)}(R_{Cl-Cl}) \tag{38}$$

where $\varepsilon_{01}^{(QM)}(R_{Cl-Cl})$ is computed from the instantaneous eigenstates calculations discussed in the previous subsection. That is, the $0 \to 1$ transition energies, $\varepsilon_{01}^{(QM)}(R_{Cl-Cl})$ (Figure 7, top panels), are the differences between the ground and first excited *instantaneous* eigenstates, as defined by eq 35, and thus, depend on the Cl−Cl stretch.

The level of agreement between the two techniques above allows one to interpret the vibrational properties using an adiabatic dressed state quantum dynamics model. Specifically, using the instantaneous eigenstates in eqs 34 and 35,

$$\Psi_0^{(QM)}(\mathbf{R}_{QM}; t) \approx \sum_n b_n(0) \exp\left[-\frac{\iota}{\hbar} \int_0^t dt' \, \varepsilon_n^{(QM)}(R_C(t')) \right]$$
$$\times \psi_n(\mathbf{R}_{QM}; R_C(t)) \tag{39}$$

Substituting eq 39 in eq 37 gives

$$I_J(\omega) = 4 \left| \sum_{i,j>i} |b_i(0)| |b_j(0)| J^{(i,j)}(\omega) \right|^2 \tag{40}$$

where

$$J^{(i,j)}(\omega) \equiv \lim_{T \to \infty} \int_{t=0}^{t=T} dt \, e^{(-\iota\omega t)}$$
$$\times \left\{ \sin\left[\phi_{ij} + \frac{1}{\hbar} \int_0^t dt' \, \Delta\varepsilon_{ij}(R_C(t')) \right] \mathbf{j}_{ij}(R_C(t)) \right\} \tag{41}$$

and

$$\mathbf{j}_{ij}(R_C(t)) \equiv \left\langle \psi_j(R_C(t)) \left| \frac{-\hbar}{m} \nabla \right| \psi_i(R_C(t)) \right\rangle \tag{42}$$

Here, we have assumed that the instantaneous eigenstates defined by eq 34 are real values in quantum nuclear configuration space. The quantity ϕ_{ij} is a phase stemming from the initial probability amplitudes, $|b_i(0)|$ and $|b_j(0)|$. We emphasize that, in this model, the transition energies $\Delta\varepsilon_{ij}$ and flux matrix elements $\mathbf{j}_{ij}$ are parametrically dependent only on the classical degrees of freedom, R_C. All time dependence in these quantities arises from the implicit dependence of R_C on t. For the 1D systems, $R_C(t) = R_{Cl-Cl}(t)$ the stretch between the

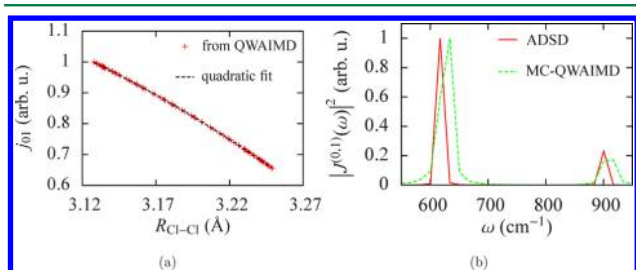Cl moieties. As noted in Figure 9, the adiabatic dressed state approximation agrees well with the full QWAIMD result.

Figure 9. (a) Plot displaying the evolution of the average flux, as computed using the adiabatic dressed state approximation (eq 42). (b) Plot comparing a spectrum obtained using the adiabatic dressed state approximation with full QWAIMD. Because of the good agreement, we interpret this dynamics as a dress-state dynamics.

Figure 9a presents the flux matrix element j_{01}, corresponding to the ground-to-first excited-state transition in the shared proton stretch, sampled every 25 fs from a 1D dynamics trajectory with nine diabatic states ($N_{DM} = 9$). The initial conditions for this simulation correspond to the choice of the ground state for the shared proton stretch (eq 29). In addition, a least-squares fit to a second-order polynomial is also provided for j_{01}. An equivalent fit is performed for the ground-to-first excited-state transition, $\Delta\varepsilon_{01}$. Figure 9b compares the flux given by the full dynamical simulation as defined by eq 37 to that predicted by the dressed state approximation in eqs 40–42. The spectral fundamentals as well as side bands that couple the asymmetric and symmetric stretches are reasonably represented by this model.

VII. CONCLUDING REMARKS

The quantum vibrational subsystem within quantum-wave-packet *ab initio* molecular dynamics (QWAIMD), which is an "on the fly" *ab initio* mixed quantum classical methodology, is represented using a basis derived from a set of Hermite Gaussian multiwavelet functions in place of the discrete grid representation used previously. This representation has the following properties: (a) reduction of polynomial order in the basis set via an hierarchical spatial rescaling, (b) analytically known expressions for the kinetic energy and free propagation operators, and (c) spatial symmetry and localization leading to sparsity and repetition in matrix representations that result in computational overhead reduction. The representation is implemented for a quantum subsystem with an arbitrary number of degrees of freedom.

A detailed performance analysis is carried out for multiple parametrization of the multiwavelet basis. Based on this analysis, a suitable choice of parametrization is subsequently benchmarked against the already-existing grid-based scheme for propagating quantum nuclei in QWAIMD. The benchmarks are carried out for one-dimensional (1D) and three-dimensional (3D) quantum dynamical representations of the shared proton motion in the $ClHCl^-$ bihalide system. In the 1D representation, separate comparisons are carried out using two levels of electronic structure theory that represent qualitatively different physical behavior for the shared proton motion. In all cases, good agreement is observed between the multiwavelet and grid-based schemes for energetic and spectral properties for multiwavelet basis sets that are significantly

smaller than the number of grid points used in the grid basis propagation scheme.

■ ASSOCIATED CONTENT

ⓢ Supporting Information

The Supporting Information describes (a) algorithmic issues related to computing the multiwavelet overlap matrix, and (b) additional numerical benchmarks that substantiate the chosen (σ_{max}, μ_{max}) values. This material is available free of charge via the Internet at http://pubs.acs.org/.

■ AUTHOR INFORMATION

Corresponding Author

*E-mail: iyengar@indiana.edu.

Notes

The authors declare no competing financial interest.

■ REFERENCES

(1) Iyengar, S. S.; Jakowski, J. *J. Chem. Phys.* **2005**, *122*, 114105.
(2) Iyengar, S. S. *Theor. Chem. Acc.* **2006**, *116*, 326.
(3) Jakowski, J.; Sumner, I.; Iyengar, S. S. *J. Chem. Theory Comput.* **2006**, *2*, 1203–1219.
(4) Sumner, I.; Iyengar, S. S. *J. Phys. Chem. A* **2007**, *111*, 10313–10324.
(5) Sumner, I.; Iyengar, S. S. *J. Chem. Phys.* **2008**, *129*, 054109.
(6) Li, X.; Iyengar, S. S. *J. Chem. Phys.* **2010**, *133*, 184105.
(7) Li, J.; Li, X.; Iyengar, S. S. *J. Chem. Theory Comput.* **2014**, DOI: 10.1021/ct5002347.
(8) Li, X.; Iyengar, S. S. *J. Phys. Chem. A* **2011**, *115*, 6269.
(9) Hocker, D.; Li, X.; Iyengar, S. S. *J. Chem. Theory Comput.* **2011**, *7*, 256.
(10) Iyengar, S. S.; Sumner, I.; Jakowski, J. *J. Phys. Chem. B* **2008**, *112*, 7601–7613.
(11) Iyengar, S. S. *Int. J. Quantum Chem.* **2009**, *109*, 3798–3810.
(12) Pacheco, A. B.; Iyengar, S. S. *J. Chem. Phys.* **2010**, *133*, 044105.
(13) Pacheco, A. B.; Iyengar, S. S. *J. Chem. Phys.* **2011**, *134*, 074107.
(14) Gerber, R. B.; Buch, V.; Ratner, M. A. *J. Chem. Phys.* **1982**, *77*, 3022.
(15) Gerber, R. B.; Ratner, M. A.; Buch, V. *Chem. Phys. Lett.* **1982**, *91*, 173.
(16) Buch, V.; Gerber, R. B.; Ratner, M. A. *Chem. Phys. Lett.* **1983**, *101*, 44.
(17) Bisseling, R. H.; Kosloff, R.; Gerber, R. B.; Ratner, M. A.; Gibson, L.; Cerjan, C. *J. Chem. Phys.* **1987**, *87*, 2760–2765.
(18) Tully, J. C. *Faraday Discuss.* **1998**, *110*, 407–419.
(19) Kapral, R.; Ciccotti, G. *J. Chem. Phys.* **1999**, *110*, 8919.
(20) Horenko, I.; Salzmann, C.; Schmidt, B.; Schutte, C. *J. Chem. Phys.* **2002**, *117*, 11075–11088.
(21) Donoso, A.; Zheng, Y. J.; Martens, C. C. *J. Chem. Phys.* **2003**, *119*, 5010.
(22) Brooksby, C.; Prezhdo, O. V. *Chem. Phys. Lett.* **2001**, *346*, 463–469.
(23) Prezhdo, O. V.; Brooksby, C. *Phys. Rev. Lett.* **2000**, *86*, 3215–3219.
(24) Gindensperger, E.; Meier, C.; Beswick, J. A. *J. Chem. Phys.* **2000**, *113*, 9369.
(25) Hammes-Schiffer, S.; Tully, J. C. *J. Chem. Phys.* **1994**, *101*, 4657.
(26) Li, R. *J. Sci. Comput.* **2005**, *24*, 321.
(27) Sumner, I.; Iyengar, S. S. *J. Chem. Theory Comput.* **2010**, *6*, 1698.
(28) Phatak, P.; Sumner, I.; Iyengar, S. S. *J. Phys. Chem. B* **2012**, *116*, 10145.

(29) Daubechies, I.; Grossmann, A.; Meyer, Y. *J. Math. Phys.* **1986**, *27*, 1271.

(30) Daubechies, I. *Ten Lectures in Wavelets*; SIAM: Philadelphia, PA, 1992.

(31) Daubechies, I. *IEEE Trans. Inform. Theory* **1990**, *39*.

(32) Strang, G.; Nguyen, T. *Wavelets and Filter Banks*; Wellesley-Cambridge Press: Wellesley, MA, 1996.

(33) Strang, G.; Strela, V. *J. Opt. Eng.* **1994**, *33*, 2104−2107.

(34) Arias, T. *Rev. Mod. Phys.* **1999**, *71*, 267−311.

(35) Johnson, B. R.; Modisette, J. P.; Nordlander, P. J.; Kinsey, J. L. *J. Chem. Phys.* **1999**, *110*, 8309−8317.

(36) Chan, Y. T. *Wavelet Basics*; Kluwer Academic Publishers: Norwell, MA, 1995.

(37) Strang, G. *SIAM J. Numer. Anal.* **1968**, *5*, 506−516.

(38) Kouri, D. J.; Zhu, W.; Ma, X.; Pettitt, B. M.; Hoffman, D. K. *J. Phys. Chem.* **1992**, *96*, 9622−9630.

(39) Hoffman, D. K.; Nayar, N.; Sharafeddin, O. A.; Kouri, D. J. *J. Phys. Chem.* **1991**, *95*, 8299.

(40) Trotter, M. F. *Proc. Am. Math. Soc.* **1959**, *10*, 545.

(41) Feit, M. D.; Fleck, J. A. *J. Chem. Phys.* **1982**, *78*, 301.

(42) Nelson, E. *J. Math. Phys.* **1964**, *5*, 332.

(43) Huang, Y.; Kouri, D. J.; Arnold, M.; Thomas L. Marchioro, I.; Hoffman, D. K. *Comput. Phys. Commun.* **1994**, *80*, 1.

(44) Kouri, D. J.; Huang, Y.; Hoffman, D. K. *Phys. Rev. Lett.* **1995**, *75*, 49−52.

(45) Feynman, R. P.; Hibbs, A. R. *Quantum Mechanics and Path Integrals*; McGraw−Hill Book Company: New York, 1965.

(46) Frazier, M.; Jawerth, B. *Indiana Univ. Math. J.* **1985**, *34*.

(47) Heil, C.; Walnut, D. *SIAM Rev.* **1989**, *21*.

(48) Balan, R. In *The Functional and Harmonic Analysis of Wavelets and Frames*; Baggett, L. W., Larson, D. R., Eds., Vol. 247 of Cont. Math.; American Mathematical Society: Providence, RI, 1999.

(49) Balan, R. In *SPIE Wavelets Applications*, Vol. *4119* of Signal and Image Processing VIII; 2000.

(50) Han, D.; Larson, D. R. *Mem. Am. Math. Soc.* **2000**, *147*.

(51) Grochenig, K.; Lyubarskii, Y. *Math. Ann.* **2009**, *345*.

(52) Führ, H. *Adv. Comput. Math.* **2008**, *29*, 357.

(53) Grochenig, K.; Lyubarskii, Y. *C. R. Acad. Sci. Paris, Ser. I* **2007**, *344*.

(54) Gabor, D. *J. Inst. Electr. Eng.* **1946**, *93*.

(55) Duffin, R. J.; Schaeffer, A. C. *Trans. Am. Math. Soc.* **1952**, *72*.

(56) Lancaster, P.; Salkauskas, K. *Curve and Surface Fitting*; Academic Press: New York, 1986.

(57) Chandler, C.; Gibson, A. *J. Approx. Theory* **1999**, *100*, 233.

(58) Riesz, F.; Sz.-Nagy, B. *Functional Analysis*; Dover Publications, Inc.: Mineola, NY, 1990.

(59) Grossmann, A.; Morlet, J.; Paul, T. *J. Math. Phys.* **1985**, *27*.

(60) Grossmann, A.; Morlet, J.; Paul, T. *Ann. Inst. H. Poincare* **1986**, *45*.

(61) Packer, J. A. In *Operator Algebras, Quantization, and Noncommutative Geometry: A Centennial Celebration Honoring John von Neumann and Marshall H. Stone*; Doran, R. S., Kadison, R. V., Eds., Vol. *365* of Cont. Math.; American Mathematical Society: Providence, RI, 2004.

(62) Wei, G. W.; Althorpe, S. C.; Kouri, D. J.; Hoffman, D. K. *J. Chem. Phys.* **1998**, *108*, 7065.

(63) Wei, G. W.; Althorpe, S. C.; Zhang, D. S.; Kouri, D. J.; Hoffman, D. K. *Phys. Rev. A* **1998**, *57*, 3309.

(64) Iyengar, S. S.; Parker, G. A.; Kouri, D. J.; Hoffman, D. K. *J. Chem. Phys.* **1999**, *110*, 10283−10298.

(65) Hoffman, D. K.; Gunaratne, G. H.; Zhang, D. S.; Kouri, D. J. *Chaos* **2000**, *10*, 240.

(66) Hu, S.; Goldman, D. I.; Kouri, D. J.; Hoffman, D. K.; Swinney, H. L.; Gunaratne, G. H. *Nonlinearity* **2004**, *17* (4), 1535.

(67) Shen, L. X.; Papadakis, M.; Kakadiaris, I. A.; Konstantinidis, I.; Kouri, D. J.; Hoffman, D. K. *IEEE Trans. Image Process.* **2006**, *15*, 1254.

(68) Iyengar, S. S.; Frisch, M. J. *J. Chem. Phys.* **2004**, *121*, 5061−5070.

(69) Helgaker, T.; Jørgensen, P.; Olsen, J. *Molecular Electronic-Structure Theory*; John Wiley and Sons, Ltd.: New York, 2000.

(70) Golub, G. H.; Loan, C. F. V. *Matrix Computations*; The Johns Hopkins University Press: Baltimore, MD, 1996.

(71) Press, W. H.; Teukolsky, S. A.; Vetterling, W. T.; Flannery, B. P. *Numerical Recipes In C*; Cambridge University Press: New York, 1992.

(72) Tolimieri, R.; An, M.; Lu, C. *Mathematics Of Multidimensional Fourier Transform Algorithms*; Springer−Verlag: New York, 1993.

(73) Szalay, P. G.; Müller, T.; Gidofalvi, G.; Lischka, H.; Shepard, R. *Chem. Rev.* **2012**, *112*, 108.

(74) Yamanaka, S.; Nishihara, S.; Nakata, K.; Yonezawa, Y.; Okumura, M.; Takada, T.; Nakamura, H.; Yamaguchi, K. *Int. J. Quantum Chem.* **2009**, *109*, 3811.

(75) Martin, R. L. *J. Chem. Phys.* **1981**, *74*, 1852.

(76) Voter, A. F.; Goddard, W. A., III. *Chem. Phys.* **1981**, *57* (3), 253−259.

(77) Jackels, C. F.; Davidson, E. R. *J. Chem. Phys.* **1976**, *64* (7), 2908−2917.

(78) Thom, A. J. W.; Head-Gordon, M. *J. Chem. Phys.* **2009**, *131* (12), 124113.

(79) Wu, Q.; Cheng, C.-L.; Van Voorhis, T. *J. Chem. Phys.* **2007**, *127*, 164119.

(80) Skone, J. H.; Pak, M. V.; Hammes-Schiffer, S. *J. Chem. Phys.* **2005**, *123*, 134108.

(81) Ayala, P. Y.; Schlegel, H. B. *J. Chem. Phys.* **1998**, *108*, 7560.

(82) Baer, M. *Beyond Born−Oppenheimer: Conical Intersections and Electronic Nonadiabatic Coupling Terms*; Wiley: New York, 2006.

(83) Hanna, G.; Kapral, R. *Acc. Chem. Res.* **2006**, *39*, 21−27.

(84) Worth, G. A.; Cederbaum, L. S. *Annu. Rev. Phys. Chem.* **2004**, *55*, 127−158.

(85) Jasper, A. W.; Zhu, C.; Nangia, S.; Truhlar, D. G. *Faraday Discuss.* **2004**, *127*, 1−22.

(86) Kendrik, B. K.; Mead, C. A.; Truhlar, D. G. *Chem. Phys.* **2002**, *277*, 31−41.

(87) Kuppermann, A. In *Dynamics of Molecules and Chemical Reactions*; Wyatt, R. E., Zhang, J. Z. H., Eds.; Marcel Dekker: New York, 1996; pp 411−472.

(88) Yarkony, D. R. *Rev. Mod. Phys.* **1996**, *68*, 985.

(89) Matsika, S.; Yarkony, D. R. *J. Am. Chem. Soc.* **2003**, *125*, 10672−10676.

(90) Arfken, G. *Mathematical Methods for Physicists*; Academic Press: New York, 1985.

(91) Kosloff, D.; Kosloff, R. *J. Comput. Phys.* **1983**, *52*, 35.

(92) Kosloff, D.; Kosloff, R. *J. Chem. Phys.* **1983**, *79*, 1823.

(93) Leforestier, C.; Bisseling, R. H.; Cerjan, C.; Feit, M. D.; Freisner, R.; Guldberg, A.; Hammerich, A.; Jolicard, D.; Karrlein, W.; Meyer, H. D.; Lipkin, N.; Roncero, O.; Kosloff, R. *J. Comput. Phys.* **1991**, *94*, 59.

(94) Neuhauser, D. *J. Chem. Phys.* **1991**, *95*, 4927.

(95) Varga, R. S. *Matrix Iterative Analysis*; Prentice−Hall: Englewood Cliffs, NJ, 1963.

(96) Gradshteyn, I. S.; Ryzhik, I. M. *Table of Integrals, Series, and Products*; Academic Press: New York, 1980.

(97) Abramowitz, M., Stegun, I. A., Eds. *Handbook of Mathematical Functions*; U.S. Government Printing Office: Washington, DC, 1964.

(98) Haberman, R. *Elementary Applied Partial Differential Equations*; Prentice−Hall: Upper Saddle River, NJ, 1998.

(99) Swalina, C.; Hammes-Schiffer, S. *J. Phys. Chem. A* **2005**, *109*, 10410.

(100) Matsunaga, N.; Chaban, G. M.; Gerber, R. B. *J. Chem. Phys.* **2002**, *117*, 3541.

(101) Jung, J. O.; Gerber, R. B. *J. Chem. Phys.* **1996**, *105*, 10332−10348.

(102) Gerber, R. B.; Ratner, M. A. *J. Chem. Phys.* **1988**, *70*, 97−132.

(103) Bowman, J. M. *Acc. Chem. Res.* **1986**, *19*, 202−208.

(104) Iyengar, S. S.; Kouri, D. J.; Parker, G. A.; Hoffman, D. K. *Theor. Chem. Acc.* **2000**, *103*, 507−517.

(105) For complex, non-Hermitian matrices more general expressions are obtained in ref 104.

2963

dx.doi.org/10.1021/ct5003016 | *J. Chem. Theory Comput.* 2014, 10, 2950−2963